





Modeling a Coronal Mass Ejection as a Magnetized Structure with EUHFORIA

G. Sindhuja¹ , Jagdev Singh¹, E. Asvestari² , and B. Raghavendra Prasad¹¹ Indian Institute of Astrophysics, Second Block, Koramangala, Bangalore—560034, India; gunvicsin11@gmail.com² Department of Physics, University of Helsinki, P.O. Box 64, FI-00014, Helsinki, Finland

Received 2021 September 22; revised 2021 November 18; accepted 2021 November 19; published 2022 January 21

Abstract

We studied an Earth-directed coronal mass ejection (CME) that erupted on 2015 March 15. Our aim was to model the CME flux rope as a magnetized structure using the European Heliospheric Forecasting Information Asset (EUHFORIA). The flux rope from eruption data (FRED) output was applied to the EUHFORIA spheromak CME model. In addition to the geometrical properties of the CME flux rope, we needed to input the parameters that determine the CME internal magnetic field like the helicity, tilt angle, and toroidal flux of the CME flux rope. According to the FRED technique geometrical properties of the CME flux rope are obtained by applying a graduated cylindrical shell fitting of the CME flux rope on the coronagraph images. The poloidal field magnetic properties can be estimated from the reconnection flux in the source region utilizing the post-eruption arcade method, which uses the Heliospheric Magnetic Imager magnetogram together with the Atmospheric Imaging Assembly (AIA) 193 Å images. We set up two EUHFORIA runs with RUN-1 using the toroidal flux obtained from the FRED technique and RUN-2 using the toroidal flux that was measured from the core dimming regions identified from the AIA 211 Å images. We found that the EUHFORIA simulation outputs from RUN-1 and RUN-2 are comparable to each other. Overall using the EUHFORIA spheromak model, we successfully obtained the magnetic field rotation of the flux rope, while the arrival time near Earth and the strength of the interplanetary CME magnetic field at Earth are not as accurately modeled.

Unified Astronomy Thesaurus concepts: [Solar physics \(1476\)](#)

1. Introduction

Coronal mass ejections (CMEs) are primary sources of geomagnetic storms and can have a great impact on the near-Earth environment and our society. Therefore, forecasting CME properties, such as arrival time and magnetic field strength and orientation, is of great importance. Coronagraph observations provide us with information like the initiation time, growth, direction, and ejection speed of CMEs. Using this information, several forecasting methods and tools have been developed to determine the interplanetary evolution of CMEs, their properties, and their arrival at Earth. To perform a Sun-to-Earth simulation of CMEs one of the key input parameters required is the magnetic field at the base of the corona, which can be obtained by extrapolating the photospheric magnetic field using for example the potential field source surface model (PFSS; Wang & Sheeley 1992; Wiegmann et al. 2017). Most of the current space weather models extend the magnetic field to the outer edge of the corona using the Schatten current sheet model (SCS; Schatten et al. 1969; Schatten 1971). The semiempirical Wang–Sheeley–Arge model is a combination of the PFSS, the SCS, and a semiempirical velocity extension (Arge & Pizzo 2000), which forms the most commonly used coronal model that extends up to 0.1 au. This model can then be coupled with magneto-hydrodynamic (MHD) models that focus on the propagation of the solar wind up to 1–2 au in what is called a heliospheric model.

The ENLIL model (Odstřil & Pizzo 1999; Odstřil et al. 2004) is one of the first MHD models used in real-time

forecasting. To simulate CMEs it uses the cone CME model, in which no internal magnetic field is considered. Therefore, in ENLIL CMEs are modeled as a hydrodynamic pulse and they are initiated usually at 21.5 or 30 solar radii. The Space-weather-forecast-usable System Anchored by Numerical Operations and Observations (SUSANOO) is a 3D MHD code developed by Shiota & Kataoka (2016). In this model, CMEs are initiated at 30 solar radii with a spheromak-like flux rope. In both ENLIL and SUSANOO models the CME speed, onset time, and position are obtained from remote-sensing observations. The Alfvén-wave Driven Solar Wind Model (AWSOM-R) + EEGGL (Jin et al. 2017) in turn starts from the surface of the Sun. The EEGGL scheme provides the input parameters for a Gibson–Low flux rope that is inserted into the AWSOM-R model to simulate a CME. The European Heliospheric Forecasting Information Asset (EUHFORIA; Pomoell & Poedts 2018) is a space weather forecasting model that aims to provide a full Sun-to-Earth modeling. It consists of a coronal and a heliospheric domain. The coronal domain extends up to 0.1 au and it consists of the low corona and upper corona. The low corona is modeled using the PFSS and the upper corona with the SCS. The heliospheric domain extends after 0.1 au until 2 au and employs an MHD model. In EUHFORIA CMEs can be modeled as a hydrodynamic pulse with the use of the cone model (Pomoell & Poedts 2018), or as magnetized CMEs by employing the linear force-free (LFF) spheromak model (Verbeke et al. 2019).

Gopalswamy et al. (2017, 2018a, 2018b, 2018c) constructed a “flux rope from eruption data” (FRED) technique by combining two key concepts: (i) the reconnection (RC) flux during an eruption is approximately equal to the poloidal flux of the ejected flux rope (Longcope et al. 2007; Qiu et al. 2007; Hu et al. 2014; Gopalswamy et al. 2018b), and (ii) white-light and extreme-ultraviolet (EUV) observations of CMEs can be



Original content from this work may be used under the terms of the [Creative Commons Attribution 4.0 licence](#). Any further distribution of this work must maintain attribution to the author(s) and the title of the work, journal citation and DOI.

used in combination with the graduated cylindrical cell (GCS; Thernisien et al. 2006, 2009) method to provide the geometric and kinematic properties of the CME (Temmer et al. 2011). In this work, we utilize the FRED technique to provide realistic input to the EUHFORIA model (Pomoell & Poedts 2018; Scolini et al. 2018; Verbeke et al. 2019).

We study the flare eruption on 2015 March 15 of a C9.1 class that commenced at 01:15 UT and peaked at 02:13 UT, according to the GOES soft X-ray light curve. This flare is associated with the CME eruption first seen in Large Angle and Spectrometric Coronagraph (LASCO; Brueckner et al. 1995) C2 on board the Solar and Heliospheric Observatory (SOHO; Domingo et al. 1995) at 01:48 UT. The first super geomagnetic storm ($Dst < -200$ nT) of solar cycle 24 was observed in the WIND spacecraft with a recorded $Dst = -223$ nT that occurred on 2015 March 17. The flare-associated CME on 2015 March 15 is the sole reason for this magnetic cloud (Wu et al. 2016). Cho et al. (2017) analyzed the in situ signatures at 1 au and found that Earth had a near flank encounter with the interplanetary flux rope. This resulted in its crossing a region of strong negative B_z for an extended period of time, which explains the strong geomagnetic storm produced.

The main aim of this work is to use the FRED technique to provide realistic input to the EUHFORIA model for simulating the CME associated with the aforementioned flare. Section 2 shows the data analysis, which describes the event selected and how we obtain the magnetic flux of the CME flux rope (poloidal and toroidal fluxes) and the geometrical properties from the GCS fitting. Section 3 describes the EUHFORIA model output obtained by the application of the FRED technique results as input to EUHFORIA. Section 4 is a discussion on the results and further action.

2. Data Analysis

The event studied in this work is the halo CME that erupted on 2015 March 15 from NOAA Active Region (AR) 12297. As mentioned in the introduction this CME eruption is associated with a C9.1-class flare that according to the GOES soft X-ray light curve started at 01:15 UT and peaked at 02:13 UT. The CME was first observed by the SOHO LASCO C2 telescope at 01:48 UT on the same day.

2.1. Post-eruption Arcade Method

Gopalswamy et al. (2017) introduced a new technique called the post-eruption arcade (PEA) method, according to which a single EUV image (193 Å) from the Atmospheric Imaging Assembly (AIA; Lemen et al. 2012) on board the Solar Dynamic Observatory (SDO; Pesnell et al. 2012) is chosen during the decay phase of the flare, when the PEA appears to be constant with time, and Helioseismic Magnetic Imager (HMI, on board SDO; Schou et al. 2012) line-of-sight (LOS) magnetograms taken near the eruption time are used to estimate the RC flux. RC flux is defined as half of the magnetic flux underlying the PEA. Gopalswamy et al. also confirmed that the RC flux is equal to the poloidal flux of the associated CME. Here we employ this PEA method to extract the RC flux for the event we investigate, and thus, the poloidal flux of the CME. To quantify the uncertainties in the selection of the PEA (see, e.g., Figure 1; the blue contour is the selected PEA overlaid on the HMI magnetogram (left) and AIA 193 Å image (right)), we repeat the selection of the PEA for 10

instances and calculate the mean and standard deviation (Sindhuja & Gopalswamy 2020). The mean is found to be $1.4e+21$ Mx and that is the measured poloidal flux and the standard deviation $2.2e+20$ is the error in the measurements. To run EUHFORIA with the spheromak CME implementation we need to convert this poloidal flux to toroidal flux. To do that we assume that the flux rope is force-free (Lundquist 1951) using Lundquist's solution,

$$\Phi_t = \Phi_r(2\pi R_0/L)J_1(x_{01})$$

where R_0 = the radius of the flux rope and $L = 2R_{\text{tip}}$ is the flux rope length. The ratio of the flux rope radius (R_0) to the leading-edge distance from the Sun center (R_{tip}) is obtained from the GCS fit. Φ_r roughly equals the poloidal flux for a force-free flux rope. x_{01} is the first zero of the Bessel function J_0 , for which we follow the method described in Gopalswamy et al. (2018b). The toroidal flux that is estimated is $5.66e+20$ Mx.

2.2. Dimming Analysis

Coronal dimmings are regions of reduced EUV and soft X-ray emission in the low corona (Hudson et al. 1996; Sterling & Hudson 1997; Thompson et al. 1998) that occur in association with CMEs. These are generally interpreted as density depletion regions caused by the evacuation of plasma during the CME liftoff (Hudson et al. 1996; Thompson et al. 1998; Harrison & Lyons 2000). Coronal dimmings are of two different types (Mandrini et al. 2005, 2007), namely core and secondary dimmings. Core dimmings depict the foot points of the flux rope observed as localized regions close to the eruption site and are located in opposite magnetic polarity regions (Harrison 1995; Hudson et al. 1996; Thompson et al. 1998; Webb et al. 2000; Gopalswamy et al. 2018c). The magnetic flux in the core dimming region is comparable to the toroidal flux of the CME flux rope (Webb et al. 2000). To start with, we identify the secondary dimming pixels by applying a threshold on logarithmic base ratio images of EUV 211 Å from SDO/AIA. A pixel is flagged as a dimming pixel when its logarithmic (\log_{10}) ratio intensity drops below -0.19 DN (digital number). This threshold was determined empirically by Dissauer et al. (2018a). The errors are estimated by changing the threshold value by $\pm 5\%$. To identify and extract the core dimming regions, we apply the minimum-intensity map technique to base difference and logarithmic base ratio images from EUV 211 Å. Each core dimming pixel fulfills the following two conditions:

- (1) It is detected in the early impulsive phase (within the first 30 minutes after the onset) of the secondary dimming.
- (2) Its pixel intensity decreases below the threshold, calculated from minimum-intensity maps of base difference and logarithmic base ratio data. These procedures are described in Dissauer et al. (2018a) and Sindhuja & Gopalswamy (2020). We have illustrated the core dimming regions in Figure 2 as blue contours in the HMI magnetogram (left) and in the AIA 211 Å (right) image. Thus from the identified core dimming regions combined with SDO/HMI magnetogram data we obtain the core dimming flux or the toroidal flux of the CME flux rope near the Sun, which is found to be $1.9e+21$ Mx.

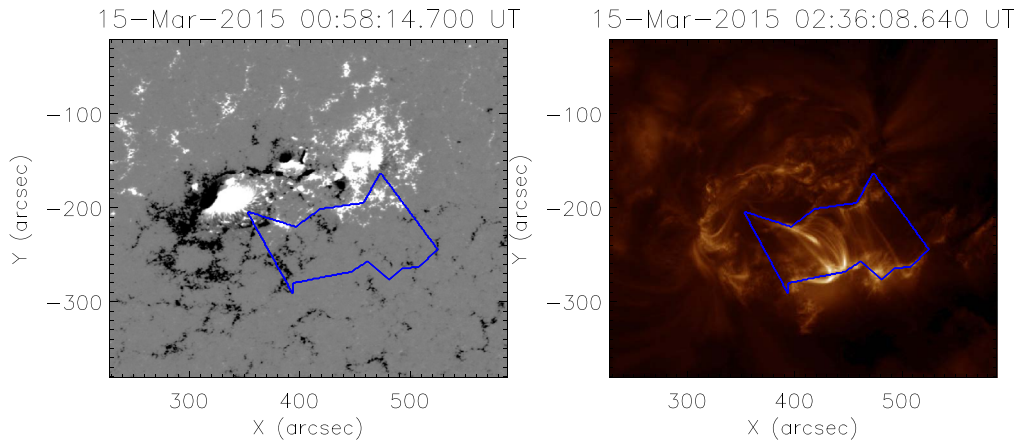


Figure 1. The eruption on 2015 March 15. (Left) SDO/HMI LOS magnetogram with the PEA overlotted. (Right) The PEA observed in the EUV image of the same region obtained at 193 \AA wavelength using AIA on board SDO with the boundaries of the arcade marked by blue lines.

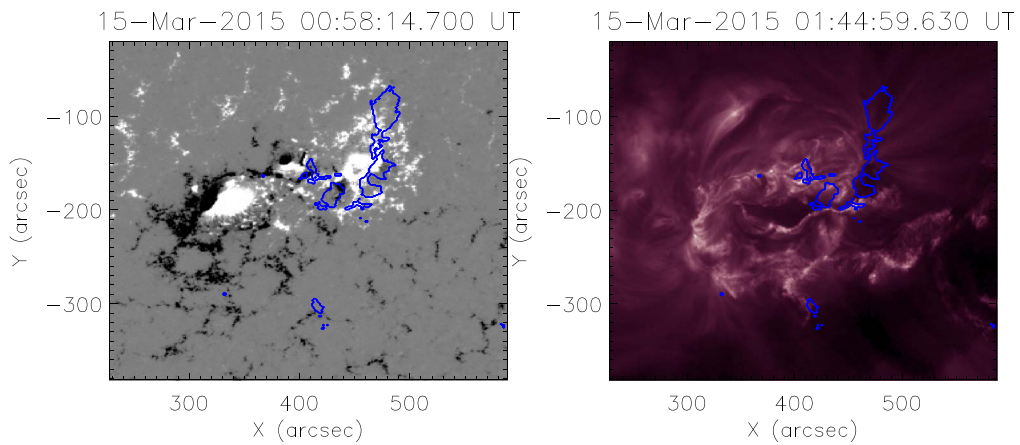


Figure 2. (Left) SDO/HMI LOS magnetogram with the dimming region overlotted. (Right) SDO/AIA 211 \AA image with potential core dimming regions (blue contours) overlotted.

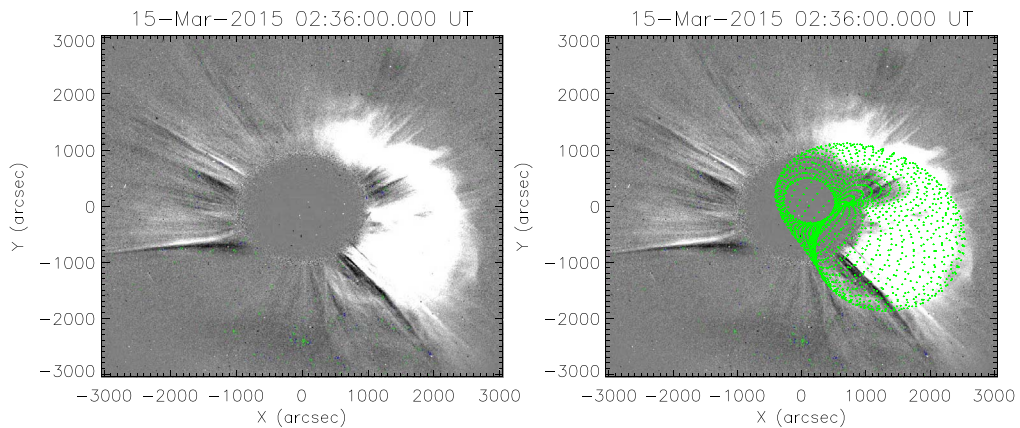


Figure 3. (Left) Difference image of the two solar coronal images obtained using the C2 coronagraph on board LASCO. (Right) The same image with the GCS fitting overlaid (green).

2.3. Geometrical Properties from GCS Fitting

To fit the flux rope, we use the GCS model (Thernisien 2011). We consider parameters such as the latitude, longitude, and tilt angle of the source region in the GCS model. We adjust parameters such as the half-angle, aspect ratio, and height of the flux rope to match the white-light images. By doing this we get the geometrical and kinematic properties of the flux rope, such as the radius R_0 ; the aspect ratio Λ , which is

$1/2 (R_{\text{tip}} - R_0) / R_0$, where R_{tip} is the heliocentric distance to the tip of the flux rope; the tilt angle; the half-angle; and the CME speed. Figure 3 illustrates the GCS fitting: before the fit (left) and after the fit (right), where a green mesh is overlaid on the SOHO/LASCO difference image.

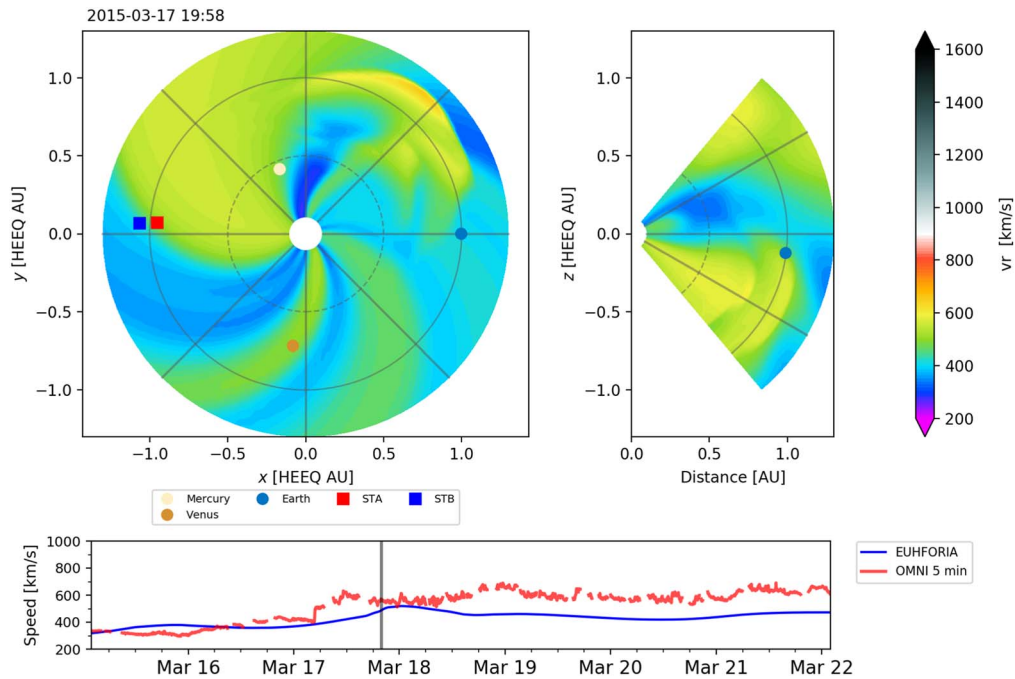


Figure 4. Snapshot of EUHFORIA RUN-1 initiated with magnetic flux equal to the toroidal flux calculated based on the observed poloidal flux estimated by the PEA analysis of the CME on 2015 March 15 at 15:58 UT. The slices show the spatial distribution of the plasma velocity in the heliographic equatorial plane (left) and in the meridional plane of Earth (right). The bottom panel shows the time series of OMNI 5 minute data (red) along with the modeled output (blue).

3. EUHFORIA Modeling Results

In EUHFORIA, spheromak CMEs are initialized at 0.1 au by specifying a set of input parameters defining the CME kinematics, geometry, and internal magnetic field. The inputs required for EUHFORIA that are obtained from the GCS fitting of the CME flux rope are the location parameter of the source region (latitude and longitude in HEEQ coordinates), the CME speed, the time at which the CME reaches 0.1 au, the half-angle, the aspect ratio, and the tilt angle. EUHFORIA is run using the face-on half-angle, which is determined following the definition in Thernisien (2011), in order to determine the spheromak radius. The parameters that determine the internal magnetic structure of the CME flux rope are the helicity sign and the magnetic flux of the flux rope. The helicity sign is the chirality of the active regions that can be inferred from their morphological features. For the event of our interest we determine that from the S-shape filament morphology, a positive helicity is injected through the photospheric surface of AR 12297 (Chandra et al. 2017; Cho et al. 2017). The toroidal flux is obtained from the core dimming regions and the poloidal flux from the PEA method. We have scheduled two runs in the EUHFORIA model. RUN-1 is initiated using the toroidal flux calculated from the poloidal PEA flux estimation, while RUN-2 is initiated using the toroidal flux estimation from the dimming analysis. In order for the magnetic field topology of the spheromak at the inner boundary of the modeling domain to better agree with that observed by LOS magnetic field measurements the tilt of the spheromak is taken to be equal to the tilt of the GCS rotated counterclockwise by 90° , similar to what was considered for the CME event studied with EUHFORIA in Asvestari et al. (2021b).

3.1. Model Output from the Different Simulation Runs

The CME is inserted at 2015 March 15 07:28 UT at a heliocentric radius of 0.1 au ($= 21.5$ solar radii) with an initial speed of 880 km s^{-1} . Observations indicate that there is no interaction with other CMEs and thus the event on 2015 March 15 is the only CME inserted in EUHFORIA. Figure 4 shows a snapshot of EUHFORIA model RUN-1 with magnetic flux equal to the toroidal flux calculated based on the observed poloidal flux that is obtained from the PEA method. The slices show the spatial distribution of the plasma velocity in the heliographic equatorial plane (left) and in the meridional plane of Earth (right), while a time series comparing the plasma speed between the EUHFORIA output and the in situ measurements by OMNI is given below. From the snapshot we can see that the modeled spheromak CME eruption propagates in the western hemisphere of the Sun as viewed from Earth and below the equatorial plane, as expected based on remote-sensing observations of the solar eruption. In the simulation results Earth is passing near the eastern flank of the CME flux rope. The near flank encounter scenario modeled by EUHFORIA is in agreement with observations that according to Cho et al. (2017) indicate that Earth crossed a strong negative B_z region at the flank of the flux rope, resulting in a strong geomagnetic storm. In Figure 5 we show the EUHFORIA time series at Earth from RUN-1 (blue solid line) and RUN-2 (cyan dashed line), together with the in situ 5 minute OMNI data (red). As can be seen RUN-1 and RUN-2 produce comparable results. The similarity of the results is possibly due to a combination of the following factors: (1) the ambient solar wind, with which the spheromak will interact in the MHD domain; (2) the remaining spheromak input parameters, which can dominate the final outcome (such as the speed, density, etc.); and (3) the fact that in the simulation Earth encounters the very edge of the spheromak and most probably the interaction region between

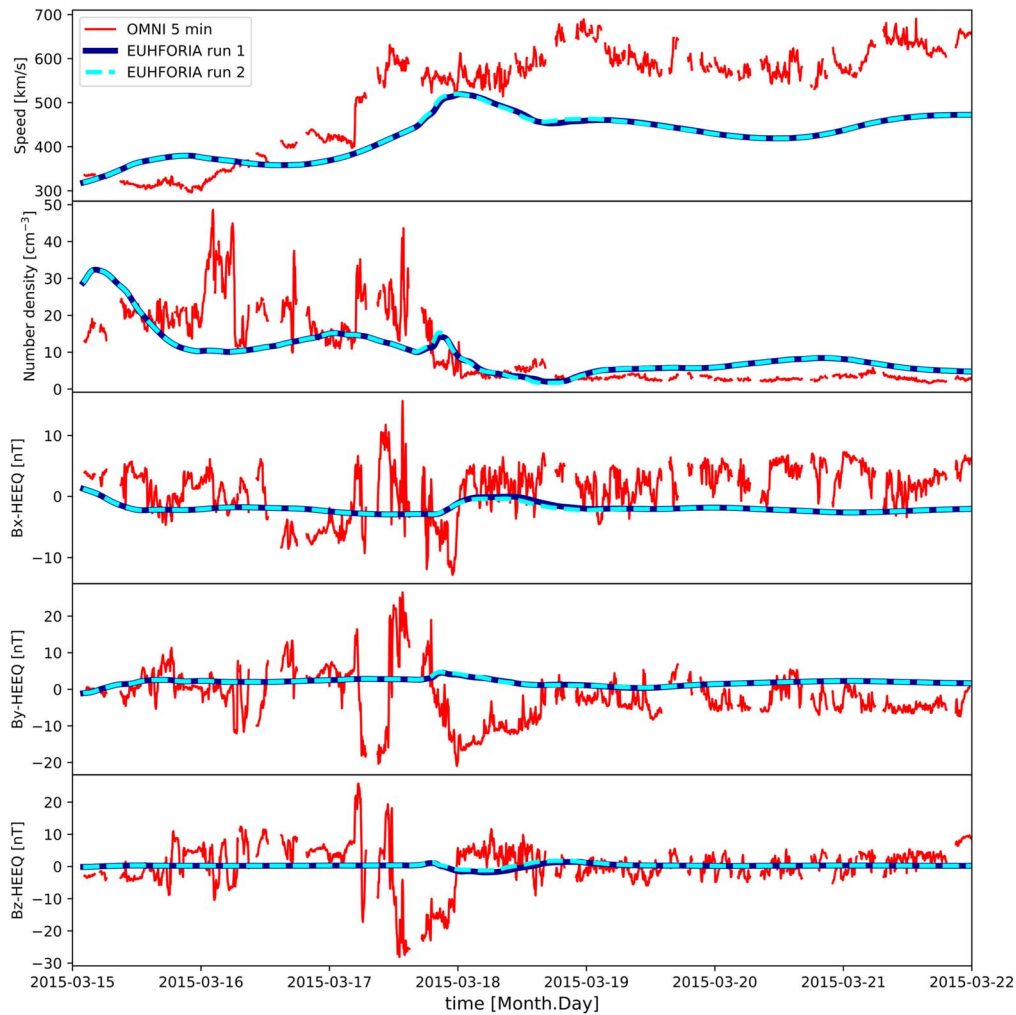


Figure 5. EUHFORIA time series for RUN-1 (blue solid line) and RUN-2 (cyan dashed line) at Earth compared to in situ 5 minute OMNI data (red). From top to bottom: speed, number density, and magnetic field strength B_x , B_y , and B_z components.

the spheromak and the ambient solar wind and not necessarily the spheromak flux rope itself.

In their paper, Kataoka et al. (2015) suggested that the interplay between the CME and a preceding corotating interaction region (CIR) was responsible for the major geomagnetic storm. In the EUHFORIA simulation there is a very weak high-speed stream (HSS) passing by Earth with which the spheromak CME is interacting. The peak velocity of the HSS is $450\text{--}500\text{ km s}^{-1}$ and it follows a slow-wind region of around 300 km s^{-1} . Therefore, indeed a weak CIR is modeled and the spheromak is interacting with it (see Figure 4). Comparing EUHFORIA and OMNI in the same figure, it is clear that the signatures arrive later in EUHFORIA than in OMNI. This can be due to the HSS not being accurately modeled in EUHFORIA in terms of arrival time and/or in terms of the peak velocity, possibly due to non-accurate coronal hole reconstruction. This is a known and studied issue in EUHFORIA (Asvestari et al. 2019, 2020; Hinterreiter et al. 2019; Samara et al. 2021). Non-accurately reconstructed HSSs and thus CIRs can lead to the discrepancies observed between OMNI and EUHFORIA. An additional factor that could have contributed to the discrepancy between the modeled flux rope structure and the one measured in situ by OMNI is the physics that govern the orientation and propagation of the spheromak, more precisely the spheromak tilting, which was recently

studied in the EUHFORIA model (Asvestari et al. 2021a). As shown in Asvestari et al. (2021a) the spheromak can experience a drift and a change to its orientation and that could have contributed further to an additional offset of the modeled spheromak employed in this event study, and thus, to the disagreement between model and observations.

According to the Richardson and Cane catalog the interplanetary CME (ICME) signature starts at 2015 March 17 13:00 UT and ends at 2015 March 18 05:00 UT, whereas in the model the ICME signature starts at 2015 March 17 20:00 UT and ends at 2015 March 18 18:00 UT. There is a delay in the disturbance from the observed and model signatures; however, this is not atypical for an MHD data driven heliospheric model and it can be due to the input parameters and magnetogram considered in the simulation. The magnetic field rotation is found to be consistent between model output and observations, even though the field strength is not well captured. The negative B_z component is also present in the simulation output. This suggests that the magnetic flux measurements are predicted well when compared between the observed and model structures. Table 1 shows the input parameters and the predicted arrival times at Earth.

Table 1
CME Input Parameters Used in the Three EUHFORIA Runs and the Predicted Arrival Times at Earth

| Parameter | RUN-1 | RUN-2 |
|------------------------|------------------------|------------------------|
| CME model | Spheromak | Spheromak |
| Insertion time | 2015/03/15 07:28 UT | 2015/03/15 07:28 UT |
| V_{CME} | 880 km s ⁻¹ | 880 km s ⁻¹ |
| Longitude (ϕ) | 47° | 47° |
| Latitude (θ) | -17° | -17° |
| Half-angle | 41° | 41° |
| Helicity sign | +1 | +1 |
| Tilt angle | -36° | -36° |
| Toroidal magnetic flux | 5.66e+20 Mx | 1.9e+21 Mx |
| Predicted ToA | 2015/03/17 20:00 UT | 2015/03/17 20:00 UT |

3.2. Exploring the Model Output at Virtual Spacecraft

To further understand why the modeled spheromak CME arrives later than the magnetic cloud observed in situ by OMNI, and why the modeled magnetic field components do not reach the observed amplitude, we place virtual spacecraft at the same orbital distance as Earth but displaced latitudinally toward the south by 5°, 20°, and 40°, and longitudinally toward the solar

west from Earth by 5°, 20°, and 40°. The choice of latitudinal displacement is made in order to investigate the interplay between the edge of the spheromak and the ambient solar wind below Earth, and how it differs from the signatures at the Earth’s location. While the longitudinal displacement helps us investigate whether indeed in the simulation Earth experiences a “very edge” encounter and how the signatures change when we go closer to a front (nose) encounter. In Figure 6 one can see that for RUN-1 the virtual spacecraft displaced south of Earth registers only minor differences in most parameters, and only a stronger difference in the B_x component. The arrival time does improve for a spacecraft displaced by 20° and 40° south. This coupled with the weak rotation seen in the magnetic field components might suggest that these virtual spacecraft are well within the sheath region while at Earth’s location the model result might suggest a shock-only crossing. In Figure 7 we present the time series of RUN-1 for virtual spacecraft displaced from Earth toward the solar west. We can see a clear improvement both in the arrival time and in the flux rope rotation for the virtual spacecraft at 40° displacement toward the solar west. This virtual spacecraft has a near front encounter with the spheromak CME. Taking into consideration the possibility that the HSS might be actually delayed in the

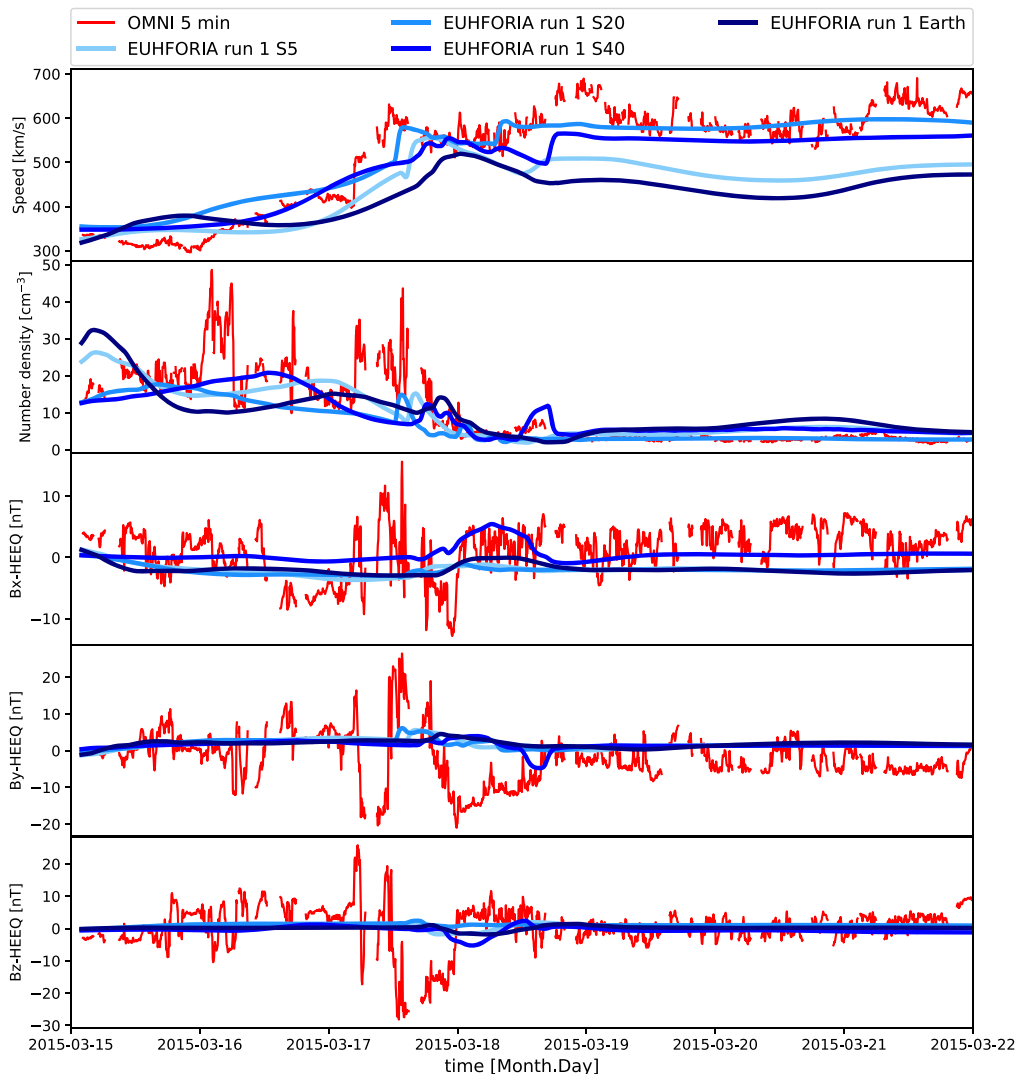


Figure 6. EUHFORIA time series for RUN-1 at different virtual spacecraft at the same orbital distance as Earth but displaced to the south of Earth by 5°, 20°, and 40°. The EUHFORIA time series at Earth is also presented for comparison together with the in situ OMNI measurements.

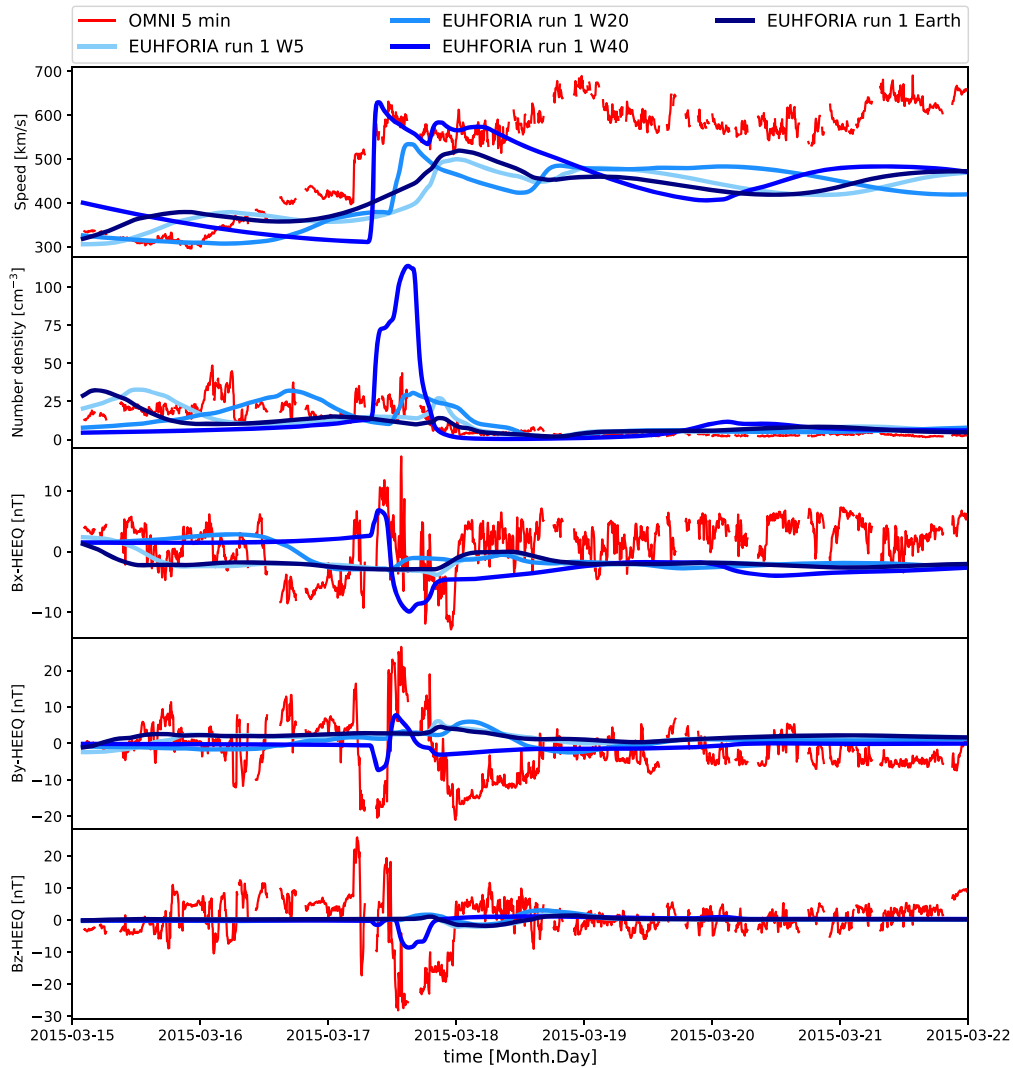


Figure 7. EUHFORIA time series for RUN-1 at different virtual spacecraft at the same orbital distance as Earth but displaced from Earth toward the solar west by 5° , 20° , and 40° . The EUHFORIA time series at Earth is also presented for comparison together with the in situ OMNI measurements.

simulations can explain why the signatures are improved so far away from Earth’s location. A more timely modeled HSS could drive the spheromak closer to Earth and result in better agreement between observed and modeled signatures. The RUN-2 output at such virtual spacecraft shows similar improvements (see supplementary material). Comparing the EUHFORIA output from the two different runs (RUN-1 and RUN-2) at the virtual spacecraft displaced from Earth’s location by 40° toward the solar west (Figure 8) we can see that the results are not as similar to each other as they are for Earth (Figure 5). In particular, the B_z component presents the strongest difference. Considering that these virtual spacecraft have a near front encounter with the spheromak CME strengthens the arguments presented in the previous section regarding the similarity of the two outputs at Earth.

4. Discussion

We have successfully applied FRED technique output to the EUHFORIA spheromak model to produce simulations of the heliospheric propagation of CMEs, their arrival time near Earth, and the internal magnetic field structure. We have shown here a case study of the CME event on 2015 March 15

associated with a C9.1-class flare. It produced the strongest geomagnetic storm of solar cycle 24. Previous work by Scolini et al. (2019) also used a modified FRED technique to obtain the magnetic flux of the CME for initiating a EUHFORIA simulation. In their work, they obtained the poloidal flux from the PEA method and then applied it to the LFF spheromak solution to obtain the axial magnetic field strength and the toroidal flux. The toroidal flux was then used in the EUHFORIA model. They used the 2012 July 12 event for their case study.

We set up two EUHFORIA runs, where RUN-1 is initiated with a toroidal flux calculated based on the estimated PEA poloidal flux, while RUN-2 is initiated with a toroidal flux extracted from the core dimming analysis. Our key conclusion is that the simulation outputs from RUN-1 and RUN-2 are comparable to each other. In addition, we conclude that they represent well the rotation of the flux rope as observed in situ by OMNI; however the magnetic field strength is not well represented. The arrival time of the modeled CME is delayed with respect to the arrival time of the ICME observed by OMNI. To further understand this we have explored the magnetic field and plasma signatures at virtual spacecraft placed at the same heliospheric distance as Earth but displaced

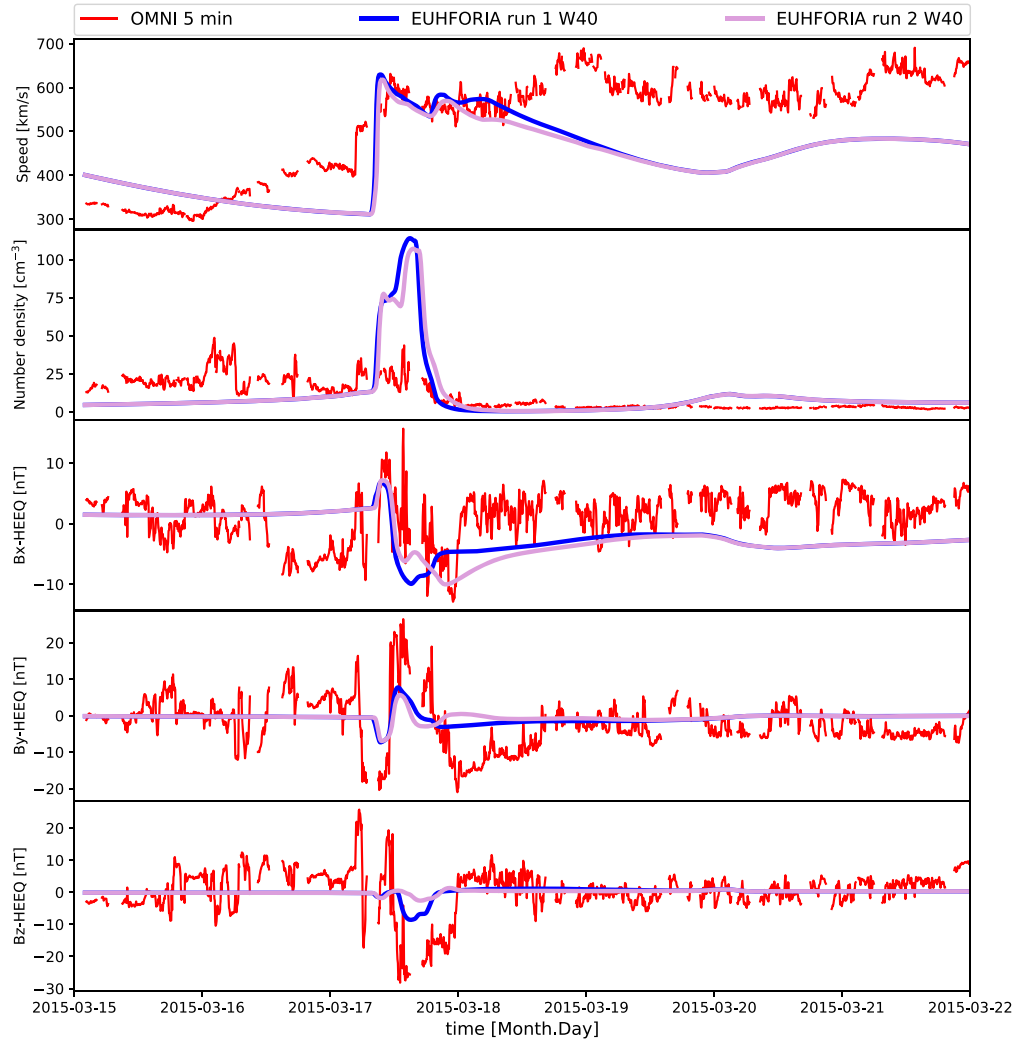


Figure 8. EUHFORIA time series for RUN-1 (blue) and RUN-2 (purple) at virtual spacecraft at the same orbital distance as Earth but displaced from Earth toward the solar west by 40° . The in situ OMNI measurements are presented for comparison.

with respect to Earth toward north/south and solar east/west. We see that virtual spacecraft having a near front encounter with the spheromak show better agreement with the OMNI observations at Earth. This could imply that the spheromak propagates further to the solar west from the Sun–Earth line than indicated by observations. Possible reasons for this are (i) a non-accurate reconstruction in EUHFORIA of the HSS with which the CME is interacting (Hinterreiter et al. 2019; Asvestari et al. 2019, 2020; Samara et al. 2021) and (ii) the spheromak tilting and drifting due to interaction with the ambient solar wind (Asvestari et al. 2021a). Further optimization of EUHFORIA simulations based on input parameters extracted from observations is necessary. This requires further testing and understanding of both models and dynamics of such events by studying more CME events. An observational program of the visible emission line coronagraph (VELC) on board ADITYA-L1, to be launched in 2022, has encouraged us to make this type of study. The VELC is capable of taking coronal images in continuum centered at 500 nm with a field of view of 1.05–3 solar radii. The images can be obtained at 30 s intervals with a pixel resolution of $2''51$. But due to restriction of the data volume that can be downloaded, the plan is to record images with pixel resolution $5''$ at an interval of 60 s for 24 hr a day (Singh et al. 2013, 2019; Raghavendra Prasad et al.

2017; Raj Kumar et al. 2018). Therefore, the CME events observed from the VELC continuum images will be used to further understand both the model and the observations. The VELC has another advantage. Simultaneously, the spectrographic observations will be taken in three emission lines, namely the 530.3 [Fe XIV], 789.2 [Fe XI], and 1074.7 [Fe XIII] nm lines. During the occurrence of the CME, enhanced emission in these emission lines is expected. In that case, the emission line profiles of these lines will provide the intensity, Doppler shift, and line width at the various locations of the CME. The continuum images of the solar corona will provide us the velocity in the plane of sky and spectroscopic observation will yield the velocity in the LOS. From the information of the location of the source region associated with the CME we can obtain the direction of the CME. Using these, we shall be able to compute the true velocity of the CME. We shall also be able to determine the temperature of the plasma of the CME from the intensity ratio of these emission lines. The information about the abovementioned parameters of the CME will help us to refine CME models further.

We thank the referee for the constructive comments and suggestions. E.A. acknowledges support from the Academy of Finland (postdoctoral researcher grant 322455). The SDO data

are courtesy of NASA/SDO and the AIA and HMI science teams. This paper has benefited from NASA's open data policy in using SOHO and SDO data and NOAA's GOES X-ray data. SOHO is a joint project of ESA and NASA. We are grateful to the US Naval Research Laboratory, CDAW Data Center, and STEREO Science Center for making the LASCO and STEREO databases available publicly.

ORCID iDs

G. Sindhuja  <https://orcid.org/0000-0002-5893-1938>

E. Asvestari  <https://orcid.org/0000-0002-6998-7224>

References

- Arge, C. N., & Pizzo, V. J. 2000, *JGR*, **105**, 10465
- Asvestari, E., Heinemann, S. G., Temmer, M., et al. 2019, *JGRA*, **124**, 8280
- Asvestari, E., Heinemann, S. G., Temmer, M., et al. 2020, *JPhCS*, **1548**, 012004
- Asvestari, E., Pomoell, J., Kilpua, E., et al. 2021b, *A&A*, **652**, A27
- Asvestari, E., Rindlisbacher, T., Pomoell, J., & Kilpua, E. 2021a, arXiv:2111.08770
- Brueckner, G. E., Howard, R. A., Koomen, M. J., et al. 1995, *SoPh*, **162**, 357
- Chandra, R., Filippov, B., Joshi, R., & Schmieder, B. 2017, *SoPh*, **292**, 81
- Cho, K. S., Marubashi, K., Kim, R. S., et al. 2017, *JKAS*, **50**, 29
- Dissauer, K., Veronig, A. M., Temmer, M., Podladchikova, T., & Vanninathan, K. 2018a, *ApJ*, **855**, 137
- Domingo, V., Fleck, B., & Poland, A. I. 1995, *SoPh*, **162**, 1
- Gopalswamy, N., Akiyama, S., Yashiro, S., & Xie, H. 2018a, *JASTP*, **180**, 35
- Gopalswamy, N., Akiyama, S., Yashiro, S., & Xie, H. 2018b, in IAU Symp., 335, *Space Weather of the Heliosphere: Processes and Forecasts*, ed. C. Foullon & O. E. Malandraki (Cambridge: Cambridge Univ. Press), 258
- Gopalswamy, N., Mäkelä, P., Akiyama, S., et al. 2018c, *JASTP*, **179**, 225
- Gopalswamy, N., Yashiro, S., Akiyama, S., & Xie, H. 2017, *SoPh*, **292**, 65
- Harrison, R. A. 1995, *A&A*, **304**, 585
- Harrison, R. A., & Lyons, M. 2000, *A&A*, **358**, 1097
- Hinterreiter, J., Magdalenic, J., Temmer, M., et al. 2019, *SoPh*, **294**, 170
- Hu, Q., Qiu, J., Dasgupta, B., Khare, A., & Webb, G. M. 2014, *ApJ*, **793**, 53
- Hudson, H. S., Acton, L. W., & Freeland, S. L. 1996, *ApJ*, **470**, 629
- Jin, M., Manchester, W. B., van der Holst, B., et al. 2017, *ApJ*, **834**, 173
- Kataoka, R., Shiota, D., Kilpua, E., & Keika, K. 2015, *GeoRL*, **42**, 5155
- Lemen, J. R., Title, A. M., Akin, D. J., et al. 2012, *SoPh*, **275**, 17
- Longcope, D., Beveridge, C., Qiu, J., et al. 2007, *SoPh*, **244**, 45
- Lundquist, S. 1951, *PhRv*, **83**, 307
- Mandrini, C. H., Nakwacki, M. S., Attrill, G., et al. 2007, *SoPh*, **244**, 25
- Mandrini, C. H., Pohjolainen, S., Dasso, S., et al. 2005, *A&A*, **434**, 725
- Odstrčil, D., Riley, P., & Zhao, X. P. 2004, *JGRA*, **109**, A02116
- Odstrčil, D., & Pizzo, V. J. 1999, *JGR*, **104**, 483
- Pesnell, W. D., Thompson, B. J., & Chamberlin, P. C. 2012, *SoPh*, **275**, 3
- Pomoell, J., & Poedts, S. 2018, *JWSC*, **8**, A35
- Qiu, J., Hu, Q., Howard, T. A., & Yurchyshyn, V. B. 2007, *ApJ*, **659**, 758
- Raghavendra Prasad, B., Banerjee, D., Singh, J., et al. 2017, *CSci*, **113**, 613
- Raj Kumar, N., Raghavendra Prasad, B., Singh, J., & Venkata, S. 2018, *ExA*, **45**, 219
- Samara, E., Laperre, B., Kieokaew, R., et al. 2021, arXiv:2109.07873
- Schatten, K. H. 1971, *CosEl*, **2**, 232
- Schatten, K. H., Wilcox, J. M., & Ness, N. F. 1969, *SoPh*, **6**, 442
- Schou, J., Borrero, J. M., Norton, A. A., et al. 2012, *SoPh*, **275**, 327
- Scolini, C., Rodriguez, L., Mierla, M., Pomoell, J., & Poedts, S. 2019, *A&A*, **626**, A122
- Scolini, C., Verbeke, C., Poedts, S., et al. 2018, *SpWea*, **16**, 754
- Shiota, D., & Kataoka, R. 2016, *SpWea*, **14**, 56
- Sindhuja, G., & Gopalswamy, N. 2020, *ApJ*, **889**, 104
- Singh, J., Bayanna, R., & Sankarasubramanian, K. 2013, *JOpt*, **42**, 96
- Singh, J., Prasad, B. R., Venkata, S., & Kumar, A. 2019, *AdSpR*, **64**, 1455
- Sterling, A. C., & Hudson, H. S. 1997, *ApJL*, **491**, L55
- Temmer, M., Veronig, A. M., Gopalswamy, N., & Yashiro, S. 2011, *SoPh*, **273**, 421
- Thernisien, A. 2011, *ApJS*, **194**, 33
- Thernisien, A., Vourlidis, A., & Howard, R. A. 2009, *SoPh*, **256**, 111
- Thernisien, A. F. R., Howard, R. A., & Vourlidis, A. 2006, *ApJ*, **652**, 763
- Thompson, B. J., Plunkett, S. P., Gurman, J. B., et al. 1998, *GeoRL*, **25**, 2465
- Verbeke, C., Pomoell, J., & Poedts, S. 2019, *A&A*, **627**, A111
- Wang, Y. M., & Sheeley, N. R. J. 1992, *ApJ*, **392**, 310
- Webb, D. F., Lepping, R. P., Burlaga, L. F., et al. 2000, *JGR*, **105**, 27251
- Wiegmann, T., Petrie, G. J. D., & Riley, P. 2017, *SSRv*, **210**, 249
- Wu, C.-C., Liou, K., Lepping, R. P., et al. 2016, *EP&S*, **68**, 151